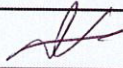
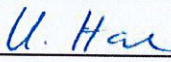


<b>GRANT AGREEMENT No.: 764902</b> <b>Project Acronym: TOMOCON</b> <b>Project title: Smart tomographic sensors for advanced industrial process control</b>			
Deliverable Rel. No. <b>D2.3.</b>	Lead Beneficiary <b>INPT / UEF</b>		
EU Del. No. <b>D7</b>	Type <b>Report</b>		
WP No. <b>WP2</b>	Date: <b>25.02.2020</b>	Revision: <b>0</b>	
<b>Innovative Training Network</b>  <b>TOMOCON</b>			
Deliverable Title  <div style="text-align: center;"> <h2>Experimental Validation Data of Improved Multiphysics Modelling</h2> </div>			
Description  <b>This deliverable is a summary description of experiments, experimental results and data obtained for multiphysics model development and validation purposes.</b>			

Prepared by:	Prof. Dr. Dominique Legendre	
Approved by:	Prof. Dr. Uwe Hampel	
Approved by Supervisory Board:		11.03.2020

Dissemination Level: **Public**



This project has received funding from the European Union's Horizon 2020 research and innovation programme under the Marie Skłodowska-Curie Grant Agreement No. 764902.

<b>TOMOCON</b>			<b>GRANT AGREEMENT No.: 764902</b>		
Deliverable Title: <b>Experimental Validation Data of Improved Multiphysics Modelling</b>					
<b>Del. Rel. No.</b>	<b>EU Del. No.</b>	<b>WP No.</b>	<b>Lead Beneficiary</b>	<b>Type</b>	<b>Date</b>
D2.3.	D7	WP2	INPT / UEF	Report	25.02.2020

Revision Sheet

<b>Revision Number</b>	<b>Purpose of Revision</b>	<b>Effective Date</b>
0	Initial Issue	11.03.2020



<b>TOMOCON</b>			<b>GRANT AGREEMENT No.: 764902</b>		
Deliverable Title: <b>Experimental Validation Data of Improved Multiphysics Modelling</b>					
<b>Del. Rel. No.</b>	<b>EU Del. No.</b>	<b>WP No.</b>	<b>Lead Beneficiary</b>	<b>Type</b>	<b>Date</b>
D2.3.	D7	WP2	INPT / UEF	Report	25.02.2020

## Table of Contents

1	Experimental data for code validation two-phase pipe flow (inline fluid separation) .....	5
1.1	Experimental data from the HZDR water / air loop flow facility .....	5
1.1.1	Description of the experimental facility .....	5
1.1.2	Measurement techniques .....	5
1.1.3	Description of the experiment .....	6
1.1.4	Data formats and repository .....	7
1.2	Experimental data from the TUL facility .....	8
1.2.1	Description of the experimental facility .....	8
1.2.2	Measurement techniques .....	9
1.2.3	Data formats and repository .....	10
2	Experimental data from tomography devices for intelligent control of drying process .....	11
2.1	Descriptions of the HEPHAISTOS oven .....	11
2.2	Process modelling .....	11
2.3	ECT sensor .....	13
2.4	Microwave tomography .....	14
2.4.1	Measurement set-up .....	14
2.4.2	Reconstruction scheme .....	15
2.5	Human-Computer Interaction .....	16
3	Experimental data for code validation liquid metal flow (continuous casting) .....	18
3.1	Experimental data from the HZDR Mini-LIMMCAST facility .....	18
3.1.1	Description of the experimental facility .....	18
3.1.2	Measurement techniques .....	18
3.1.3	Data formats and repository .....	20
4	Experimental data for code validation of particle formation in semibatch crystallization process .....	22
4.1	Experimental data from LUT continuous carbon capture and crystallization units .....	22
4.1.1	Description of the experimental facility .....	22
4.1.2	Measurement techniques .....	23
4.1.3	Description of the experiment .....	23
4.1.4	Data formats and repository .....	25
5	Experimental data for the saturated sucrose solution and crystals observation .....	27
5.1	Experimental data from Process tomography laboratory at Technical University of Lodz .....	27
5.1.1	Description of the Electrical Resistance Tomography (ERT) experimental facility .....	27



<b>TOMOCON</b>			<b>GRANT AGREEMENT No.: 764902</b>		
Deliverable Title: <b>Experimental Validation Data of Improved Multiphysics Modelling</b>					
<b>Del. Rel. No.</b>	<b>EU Del. No.</b>	<b>WP No.</b>	<b>Lead Beneficiary</b>	<b>Type</b>	<b>Date</b>
D2.3.	D7	WP2	INPT / UEF	Report	25.02.2020

5.1.2	Measurement techniques in ERT .....	28
5.1.3	Data formats and repository .....	29
6	References .....	30



<b>TOMOCON</b>				<b>GRANT AGREEMENT No.: 764902</b>	
Deliverable Title: <b>Experimental Validation Data of Improved Multiphysics Modelling</b>					
Del. Rel. No.	EU Del. No.	WP No.	Lead Beneficiary	Type	Date
D2.3.	D7	WP2	INPT / UEF	Report	25.02.2020

# 1 Experimental data for code validation two-phase pipe flow (inline fluid separation)

## 1.1 Experimental data from the HZDR water / air loop flow facility

### 1.1.1 Description of the experimental facility

Inline fluid separation data was produced experimentally using the facility shown in Figure 1. The horizontal test section is made of acrylic glass and has an inner diameter of  $D=50$  mm. It is supplied with deionized water by a centrifugal pump and air from the compressed air line of the laboratory. The volumetric flow rates of incompressible liquid are manually adjusted by controlling the speed of the pump and subsequently measured with magnetic-inductive flow meters in order to determine the superficial liquid velocities. The separation of the phases is done by a swirl element. The initial CAD (computer-aided design) blueprint of the swirl element was provided by Delft University of Technology and later adjusted at HZDR. The new blueprint was used to 3D print the swirl element in order to fit inside the pipe of the experimental setup. Material used for the 3D printed design is Polyamide 12. The length of the horizontal combination of acrylic glass and plastic pipes presented in Figure 1 is  $L=5$  meters.

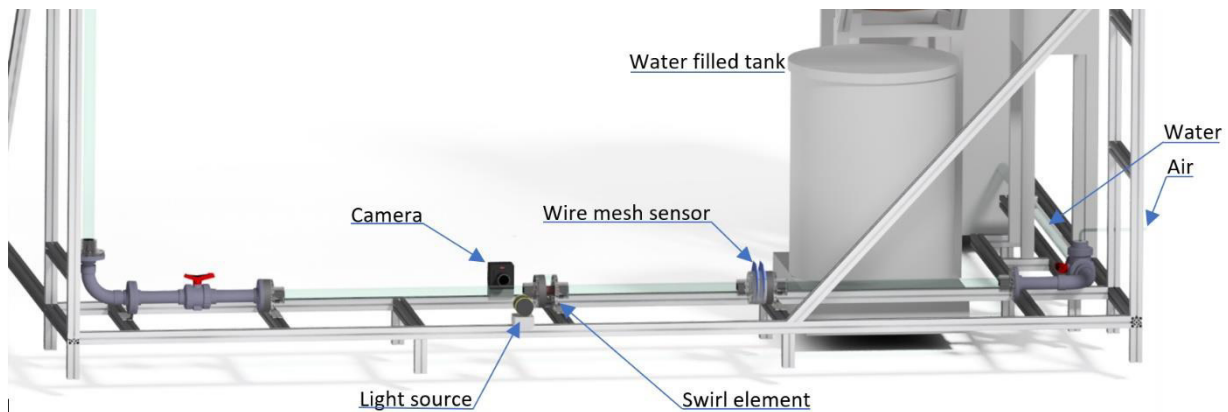


Figure 1: Experimental setup with upstream WMS and downstream camera and light source (CAD render)

A wire-mesh sensor is mounted at  $53 L/D$  downstream the last elbow in order to measure a sufficiently developed two-phase flow. The swirl element is placed after further  $4 L/D$ . A high-speed camera was installed at  $2 L/D$  downstream the swirl element tail in order to record the gas core dynamics. On the opposite there is a LED light source illuminating the developed gas core. Transparent pipes are used for the ease of camera recording and visual observation.

Experiments were performed in an operating range of practical interest, i.e. close to industrial scenarios. Some of the higher flow rates could not be achieved due to the operational limit of the pump and physical characteristics of the pipe. Pressure and temperature transducers further complement the instrumental part upstream of the swirl element to yield additional dynamic pressure drop information for parameters considered to have an influence on the gas core behavior. The process was controlled and monitored by a programmable logic controller.

### 1.1.2 Measurement techniques

The high-speed camera records the flow downstream the swirl, that is, the gas core. Images were taken with a frequency of 250 frames per second for a total time of 12 seconds per experiment giving 3,000 frames per experimental point in total. Care was given to avoid reflections in the wall of the pipe. In this configuration, the gas core appears as a semitransparent shadow in the images. Due to the optimized video setup, no additional



TOMOCON				GRANT AGREEMENT No.: 764902	
Deliverable Title: <b>Experimental Validation Data of Improved Multiphysics Modelling</b>					
Del. Rel. No.	EU Del. No.	WP No.	Lead Beneficiary	Type	Date
D2.3.	D7	WP2	INPT / UEF	Report	25.02.2020

techniques for image pre-processing like contrast adjustment or brightness modification had to be applied to the images. Post processing of the images was done using MATLAB and is schematically shown in Figure 2.

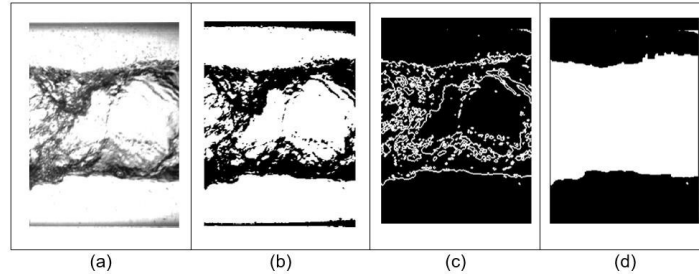


Figure 2: Illustration of the camera image processing steps a) Original image, b) Binarized image, c) Extracted boundaries after application of an edge operator, d) Binarized core after flood-fill

Developed algorithms in addition with digital image segmentation techniques were applied on the raw camera images. Pixel values in the output image (Figure 2d) can be count and expressed in length units. One pixel of the output image is 0.19 mm in reality. Characterizing gas core parameters calculated using image information are the average gas-core diameter, the standard deviation of the produced gas core and the frequency of fluctuation of the gas core diameter around the mean diameter.

For upstream data acquisition processing, we used a conductivity wire-mesh sensor. A camera is not applicable here as the highly-disperse bubbly flow is opaque. A wire-mesh sensor consists of two planes of parallel wires in the pipe cross-section. They are separated by a short distance and arranged so that they form an angle of 90° to each other. In the one plane (transmitter), wires are sequentially activated with a voltage while at the (receiver) wires in the other plane transmitted electrical currents are simultaneously sampled. This way the electrical conductivity in the crossing-points is obtained with high speed, i.e. 10,000 frames per second in our case. In a first approximation the local void fraction in a crossing with indices  $i, j$  and  $n$  the sample number is

$$\varepsilon_{i,j,n} = 1 - \frac{U_{i,j,n}^{meas}}{U_{i,j}^W} \quad (1)$$

where  $U_{i,j,n}^{meas}$  denotes the local instantaneous sensor signal of the measured value measured and  $U_{i,j}^W$  the time averaged sensor signal of the calibration measurement. In our study, we were interested in the mean local void fraction

$$\overline{\varepsilon}_{i,j} = \frac{1}{N} \sum_{n=1}^N \varepsilon_{i,j,n} \quad (2)$$

with  $\varepsilon_{i,j,n}$  denoting the measured void fraction in the crossing  $i, j$  for the total number of samples  $N$  and furthermore in the total average void fraction

$$\bar{\varepsilon} = \sum_i \sum_j a_{i,j} \overline{\varepsilon}_{i,j}, \quad (3)$$

where  $a_{i,j}$  is a weight coefficient that denotes the share of a crossing point with the cross-section. Effectively  $a_{i,j}$  accounts for a lower share of crossing points at the pipe boundary.

### 1.1.3 Description of the experiment

Experiments were performed for different gas and liquid flow rates which are further expressed in terms of superficial velocities  $J_{sg}$  and  $J_{sl}$ , respectively. The volumetric flow rate of the water  $\dot{V}_l$  was adjusted by speed control of the pump and measured by magnetic-inductive flow meters. The superficial velocity is then obtained from



<b>TOMOCON</b>				<b>GRANT AGREEMENT No.: 764902</b>	
Deliverable Title: <b>Experimental Validation Data of Improved Multiphysics Modelling</b>					
<b>Del. Rel. No.</b>	<b>EU Del. No.</b>	<b>WP No.</b>	<b>Lead Beneficiary</b>	<b>Type</b>	<b>Date</b>
D2.3.	D7	WP2	INPT / UEF	Report	25.02.2020

$$J_{sl} = \frac{\dot{V}_l}{A} \quad (4)$$

where  $A$  denotes the cross-sectional area of the pipe. Since air is a compressible fluid, its superficial velocity was adjusted by the means of mass flow controllers while accounting for temperature  $T_g$  and local gauge pressure  $p_{rel}$ :

$$J_{sg} = \frac{\dot{V}_{g,s} T_g}{A T_S (p_{amb} + p_{rel})} \quad (5)$$

Here,  $\dot{V}_{g,s}$  denotes the volumetric gas flow rate at standard conditions  $p_S$  and  $T_S$ , and  $p_{amb}$  is the ambient pressure. The onset of stable gas core formation was identified at a superficial liquid velocity of approximately 0.6 m/s.

Obtained measurement data was analyzed to find behavioral correlation in two-phase mixture upstream and swirl flow downstream. Figure 3 shows the average diameter of the gas core for the variation of superficial liquid and gas velocities. Expectedly, the average core diameter generally increases with rising superficial gas velocity, or more precisely higher gas flow rate. However, the behavior with respect to the superficial liquid velocity is not uniform. While lower gas flow rates show increasing core diameters with increasing liquid flow rates, the opposite trend is obtained for the highest superficial gas velocity of  $J_{sg} = 0.46$  m/s. Additionally, the core diameter obviously tends to get almost independent of the gas flow rate at higher superficial liquid velocities.

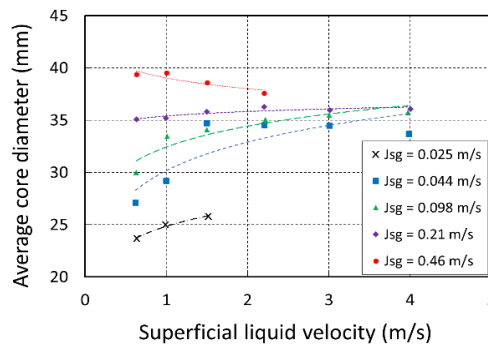


Figure 3: Average gas-core diameter in dependence of superficial velocities of liquid and gas

Besides the influence of the upstream flow pattern, a stabilization of the gas core is generally observed with increasing superficial liquid velocity. The change in pressure difference within each fluid in radial direction downstream is much smaller than the actual difference between the two fluids according to Slot [1]. Results from the observed gas core behavior were compared to the results of these findings for an additional estimation of the validity. The highest pressure is measured close to the swirl element near the wall, while the lowest pressure is close to the swirl in the center. Due to a much higher difference in pressure between the fluids, the increase in gas flow will not allow the gas core to expand further even if the initial void fraction of the upcoming flow is higher. Moving further downstream, this effect of pressure difference and losing momentum will be less due to friction. The two separated fluids would eventually merge downstream, thus the reason for mounting the camera near the swirl element. However, the gas core diameter also expands having a lower superficial gas velocity while gradually increasing its superficial liquid velocity.

Further analyzing the obtained data has resulted with an outcome that the wire-mesh sensor can predict the average gas core downstream within a range of +/-10 %.

#### 1.1.4 Data formats and repository

All of the experimental data including a description of the stored files are uploaded in the "Rosendorf Data Repository" (RODARE). Measurement readings are stored and divided into 34 measurement folders. Each fold-



TOMOCON			GRANT AGREEMENT No.: 764902		
Deliverable Title: <b>Experimental Validation Data of Improved Multiphysics Modelling</b>					
Del. Rel. No.	EU Del. No.	WP No.	Lead Beneficiary	Type	Date
D2.3.	D7	WP2	INPT / UEF	Report	25.02.2020

er contains data from a wire-mesh sensor, high-speed camera recording and readings from the volumetric flow instruments, pressure and temperature sensors. The wire-mesh sensor provides two files per measurement point. The first one in “txt” format stores information containing physical and measurement characteristics of the sensor like temporal and spatial resolution, acquisition rate etc. The second file is the raw sensor data having stored the local conductivity of each cross section of the transmitter and receiver wires of the wire-mesh sensor. The stored data is rearranged as a single column with each row of that column containing 4 bytes or 32 bits. The data type for each row is DWORD.

Camera recordings are in “avi” format and the additional file is the camera settings. It is in a format that can be read only by the software of the cameras manufacture. The “csv” file in each folder is a collection of flow rate, temperature and pressure readings for the corresponding measurement point.

## 1.2 Experimental data from the TUL facility

### 1.2.1 Description of the experimental facility

The experiments were performed using the two-phase liquid / gas flow facility of the Tom Dyakowski Process Tomography Laboratory at Lodz University of Technology (TUL). The liquid / gas flow facility consists of horizontal and vertical flow loops of three different pipe dimensions (outer diameters: 90 mm, 50 mm, and 30 mm), as shown in Figure 4a. The loop consists of a buffer tank, followed by a centrifugal pump and a flow meter. Tap water is used in the installation, as agreed with members of the inline fluid separation demonstration group. A compressor of 5 bar capacity was used to produce gas, and it was injected in the flow installation using the Brooks Mass Flow Controller (MFC). The valve operations and Brooks control were carried out using National Instruments (NI) system. The experiments were conducted using the vertical flow installation shown in Figure 4b.

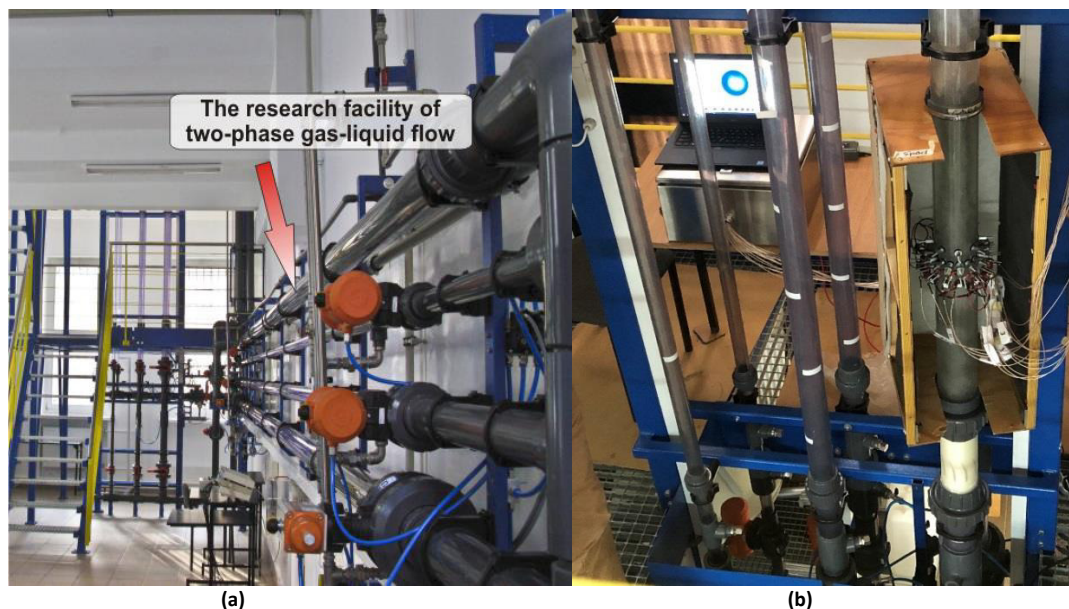


**Figure 4: (a) Tom Dyakowski Process Tomography Laboratory horizontal and vertical liquid / gas flow loop (b) Vertical flow installation with swirl element and ERT sensor mounted on the 90 mm pipe. The figure also shows in the back the live ERT image reconstruction module from TomoKisStudio and the ROCSOLE FlowWatch device.**

The installation was modified in a modular manner such that different sensors could be tested without causing harm to the rest of the structure. The swirl element with a vane angle of 38.1° (Star-2014) was placed on the 90 mm outer diameter pipe and 1 m above the water injection point. For experiments, single and two-layered



<b>TOMOCON</b>				<b>GRANT AGREEMENT No.: 764902</b>	
Deliverable Title: <b>Experimental Validation Data of Improved Multiphysics Modelling</b>					
<b>Del. Rel. No.</b>	<b>EU Del. No.</b>	<b>WP No.</b>	<b>Lead Beneficiary</b>	<b>Type</b>	<b>Date</b>
D2.3.	D7	WP2	INPT / UEF	Report	25.02.2020

sensing strategies were used and they were mounted 500 mm above the swirl element. The specifications of each sensor are described in Table 1.

**Table 1: Sensor specifications**

	Sensor 1	Sensor 2
<b>Number of Layers</b>	1	2
<b>Number of Electrodes Per Layer</b>	16	8
<b>Electrodes Material</b>	Stainless Steel	Stainless Steel
<b>Head Size</b>	12 mm	12 mm
<b>Thread Size</b>	5 mm	5 mm
<b>Distance Between Each Electrode</b>	2.7 mm	5.4 mm

The experiments were conducted using the electrical tomography system developed at the Research and Development facility of ROCSOLE Ltd Finland. It is worth mentioning that the system also uses unique signal conditional units mounted on the electrodes to assure the adequate electrical response. A high-speed camera from Basler, together with illuminating light sources, was installed at the level of sensors to validate the results obtained by both sensors. The TUL developed software TomoKisStudio was used for live image reconstruction and raw data recording.

### 1.2.2 Measurement techniques

Twenty-five experimental points were explored in 3 sets of experiments. The experiments consist of a combination of 5 liquid velocities and 5 gas velocities at room temperature. Both ranges were varied between 10 m<sup>3</sup>/h and 30 m<sup>3</sup>/h, in steps of 5 m<sup>3</sup>/h. This approach results in superficial velocities varying between 0.5 and 1.5 m/s, in steps of 0.25 m/s. The flow map is shown in Figure 5a.

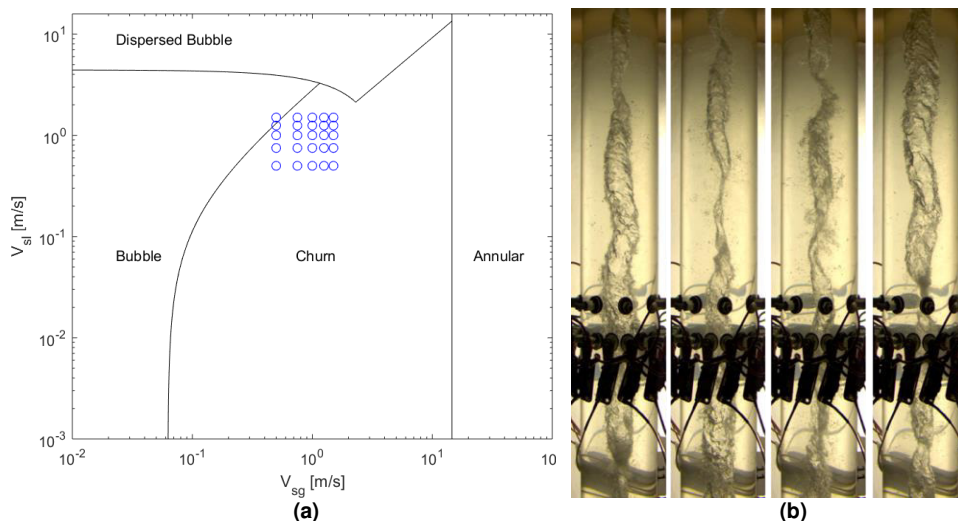


**Figure 5: (a) Flow Map, (b) Sequence of high-speed images at a liquid flow rate of 0.75 m/s and a gas flow rate of 0.50 m/s**

The 3 sets of experiments consist of:

- I. A set of flow images obtained at 50 fps with flow measurements by a single layer 16-electrode ERT sensor placed 500 mm downstream of the swirl element. The ERT was operating at approximately



TOMOCON			GRANT AGREEMENT No.: 764902		
Deliverable Title: <b>Experimental Validation Data of Improved Multiphysics Modelling</b>					
Del. Rel. No.	EU Del. No.	WP No.	Lead Beneficiary	Type	Date
D2.3.	D7	WP2	INPT / UEF	Report	25.02.2020

12 Hz, and 1 minute of raw data was recorded using TomoKisStudio. Due to the memory occupied by the fast camera images, only the last 10 seconds were captured, always starting when the ERT reaches about 600 measurements. An example of the captured images is shown in Figure 5b.

- II. The second set of images was obtained at 50 Hz, but for this set of experiment the ERT sensor consists of 2 layers of 8 electrodes each. The bottom layer was at the same location (500 mm above the swirl element), and the second layer was placed 530 mm above it. The same conditions were considered, i.e., 1-minute recording of raw data at 12 fps, with imaging starting at 600 frames.
- III. The last set of measurements consists of flow images at 100 fps, without any ERT installed in the loop, for better optical visualization of the flow. Again, only 10 s for each condition were recorded.

During the experiments, the air injection was set first. The MFC presents an internal controller that adjusts it in relation to a reference value. The pump frequency was then manually adjusted, and the measurements only started when a considerably stable flow rate was achieved.

To accurately estimate the radius of the vortex, some static measurements were also performed using both 16 electrodes single plane and twin layered 8 electrode sensors. Tests were done by placing hollow phantoms ranging from 10 mm to 50 mm diameters at different positions inside the sensing area, to simulate gas core formation. The recorded data from both static and dynamic measurements are being processed for radius retrieval using image reconstruction and raw data processing techniques.

### 1.2.3 Data formats and repository

The data from the experimental campaign of TUL is uploaded on Onedrive and can be accessed using the following URL:

[https://tulodz-my.sharepoint.com/:f/g/personal/muhammad\\_sattar\\_p\\_lodz\\_pl/EnEYQjBBwx5BrtKUKehN MwYBHS87yt5wsqp1azDzN8KiKq?e=tMwgrA](https://tulodz-my.sharepoint.com/:f/g/personal/muhammad_sattar_p_lodz_pl/EnEYQjBBwx5BrtKUKehN MwYBHS87yt5wsqp1azDzN8KiKq?e=tMwgrA)

The data is stored in three different folders, named as *ERT*, *Fast Camera Analysis*, and *Flow analysis*.

- ERT: This folder contains three subfolders named as :
  - 1x16: Contains data of single layer 16 electrode ERT sensor,
  - 2x8: Contains data of twin layer 16 electrode ERT sensor,
  - Static: Contains data of static measurements.
- Fast Camera Analysis: This folder has all the images from each experimental point at 50 fps recorded simultaneously with the sensor as described in the section above.
- Flow analysis: This folder contains images obtained at 100 fps without the ERT measurements.

The raw data in the ERT folder is stored in ".txt" in the form of a NxM matrix where N(=720) represents the total number of frames and M(=120) is the number of electrode pair measurements for one frame. Images recorded from the camera are in the ".tiff" format with the resolution of 1920x500px. The base folder also contains a readme file containing a detailed description of the data and also an excel sheet describing all the notations and experimental conditions.

#### **Important note:**

The ERT data is deliberately kept with the raw format. It is upon the decision between the different parties responsible for modelling and experimentation to decide which data processing needs to be performed to make the comparison possible.



TOMOCON			GRANT AGREEMENT No.: 764902		
Deliverable Title: <b>Experimental Validation Data of Improved Multiphysics Modelling</b>					
Del. Rel. No.	EU Del. No.	WP No.	Lead Beneficiary	Type	Date
D2.3.	D7	WP2	INPT / UEF	Report	25.02.2020

## 2 Experimental data from tomography devices for intelligent control of drying process

### 2.1 Descriptions of the HEPHAISTOS oven

The microwave drying system (HEPHAISTOS) oven as shown in Fig. 6 (left) was built at KIT with the help of Vötsch Industrietechnik, Reiskirchen, Germany. The system Hybrid VHM180/300, with a diameter of 1 m and 4 m in depth, consists of three module with six magnetrons in each module. Each magnetron works at 2.45 GHz with 2 kW output power, which is coupled into the oven with slotted waveguide antennas. To improve the uniformity of the electromagnetic fields distribution, the applicator was designed with a hexagonal cross section as shown in Fig. 6 (right).

The drying process is performed by generating a high electromagnetic power inside the oven. In addition, there is a running conveyor belt inside this oven, which moves with a constant speed  $v_0$  (can be adjusted between 0.13 m/min up to 6.75 m/min) and carries the product. Here, the wet product inside the oven is an impregnated foam provided by the PINTA Company. The final goal is to reach a moisture level equal or less than  $15\% \pm 2$  all over inside the foam.



Figure 6: (left) Microwave HEPHAISTOS oven, (right) inside the oven with the hexagonal cross section

During the drying process of polymer foam with microwaves, the problem of hotspot and thermal runaway conditions must be solved. One way to solve this problem is by selectively heating the sample, i.e. to control the power of the magnetrons to conduct the power into the wet area inside the foam and at the same time reduce the energy and time of the process. However, applying such a precise microwave power control requires non-invasive in-situ measurement of the unknown distribution of moisture inside the material. Thus, microwave tomography and electrical capacitance tomography sensors are integrated with the oven to estimate the moisture content distribution inside the foam. This information will further be used by the controller to achieve selective heating.

### 2.2 Process modelling

Process models are used for several tasks such as simulations and control design. There are various techniques to model a process. One approach is first-principles modelling in which the physics and math behind the process is known. Therefore, the model can be developed using these principles. The second technique is called data-driven modelling or system identification. In this technique, there is no knowledge of the details of the system. However, there is measured data available. Using this data, a model can be reconstructed for the system.

For the microwave drying process, a process model based on the physics behind it has been already developed. The details of this model are as follows.



TOMOCON				GRANT AGREEMENT No.: 764902	
Deliverable Title: <b>Experimental Validation Data of Improved Multiphysics Modelling</b>					
Del. Rel. No.	EU Del. No.	WP No.	Lead Beneficiary	Type	Date
D2.3.	D7	WP2	INPT / UEF	Report	25.02.2020

To describe the heat and mass transfer in the foam inside the cavity, the proposed coupled PDEs for the mathematical description of heat and mass transfer in capillary-porous bodies are modified and extended to model the microwave drying process. These equations are

$$\frac{\partial}{\partial t} \left[ \frac{\rho M}{100} \right] = \vec{\nabla} \cdot \left[ \left( \frac{k_m \delta}{c_m} \right) \nabla T + \frac{k_m}{100 c_m} \vec{\nabla} M \right], \quad (6)$$

$$\frac{\partial}{\partial t} [\rho c_q T] = \vec{\nabla} \cdot \left[ \left( k_q + \frac{\mu \lambda k_m \delta}{c_m} \right) \nabla T + \frac{\mu \lambda k_m}{100 c_m} \vec{\nabla} M \right] + P_{mw}^n u, \quad (7)$$

where  $M$  is the moisture content percentage,  $T$  is the temperature,  $k_m$  is the moisture conductivity,  $k_q$  is the thermal conductivity of the moist material,  $c_m$  is the moisture capacity,  $c_q$  the heat capacity,  $\delta$  is the thermal gradient coefficient,  $\rho$  is the density,  $\lambda$  is the latent heat of vaporization and  $\mu$  is the ratio of the vapor diffusion coefficient to the coefficient of total moisture diffusion.

The last term in Eq. (7) describes the effect of microwave heating. The boundary conditions for the PDEs (6)-(7) are described by

$$-k_q \frac{\partial T}{\partial n} = h_q (T - T_g) + \frac{(1-\mu)\lambda h_m}{100 c_m} (M - M_g), \quad (8)$$

$$\frac{-k_m}{100 c_m} \frac{\partial M}{\partial n} = \left( \frac{k_m \delta}{c_m} \right) \frac{\partial T}{\partial n} + \frac{h_m}{100 c_m} (M - M_g), \quad (9)$$

where  $h_q$  is the convective heat transfer coefficient,  $h_m$  is the convective mass transfer coefficient,  $M_g$  is the ambient air moisture content and  $T_g$  is the ambient air temperature. The drawback of this model is that some of the model parameters are not known for the foam. Therefore, the second technique of process modelling which is system identification using measured data is chosen to be utilized. By having this model, we can either use the identified model to design the controller or we can use it to validate the developed mathematical model.

For system identification, sufficiently rich signals are given as the power levels of the magnetrons which are the system inputs and the system output which is the foam moisture measured by the ECT sensor. Fig. 7 shows this scheme. Sufficiently rich signals are the kind of signals which have the necessary conditions to identify all the system parameters. An adaptive pseudorandom binary sequence (APRBS) signal is one of the suitable candidates for identifying nonlinear systems. Fig. 8 shows an example of this signal.

The ECT sensor has been already designed, built and installed on the microwave system, to run several experiments to measure enough data for the system identification. Before installing the sensor, several experiments have been conducted to ensure the performance of the sensor which will be explained in section 2.4. The experiments after installing the sensor for system identification are scheduled for March 2020.

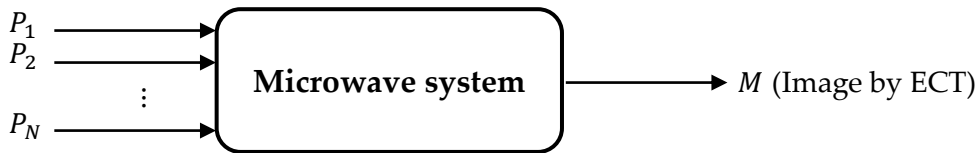


Figure 7: The system identification scheme



TOMOCON			GRANT AGREEMENT No.: 764902		
Deliverable Title: <b>Experimental Validation Data of Improved Multiphysics Modelling</b>					
Del. Rel. No.	EU Del. No.	WP No.	Lead Beneficiary	Type	Date
D2.3.	D7	WP2	INPT / UEF	Report	25.02.2020

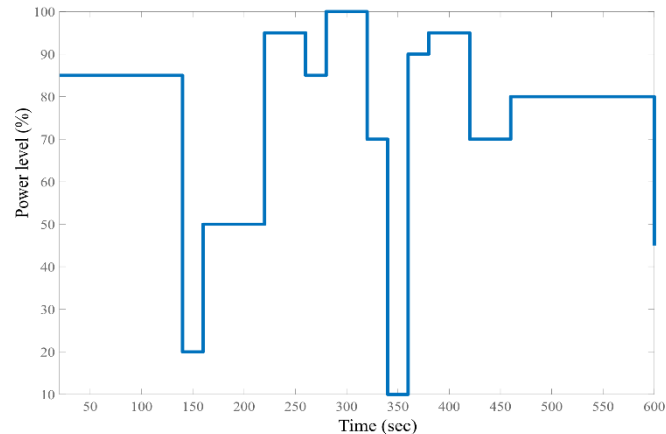


Figure 8: APRBS signal as the system input

## 2.3 ECT sensor

The ECT sensor consists of several electrodes mounted around the target. By applying electrical voltage to one of the electrodes, the electrical capacitances between the other electrodes are measured. By repeating this measurement procedure and having each of the electrodes as a source, the electrical permittivity of the target can be reconstructed. Fig. 9 shows the designed and built ECT sensor for this demonstration using 12 electrodes on the top and bottom surfaces. MATLAB and Netgen software are used to design the sensor geometry and create its mesh. The reconstruction algorithm is also solved in MATLAB.

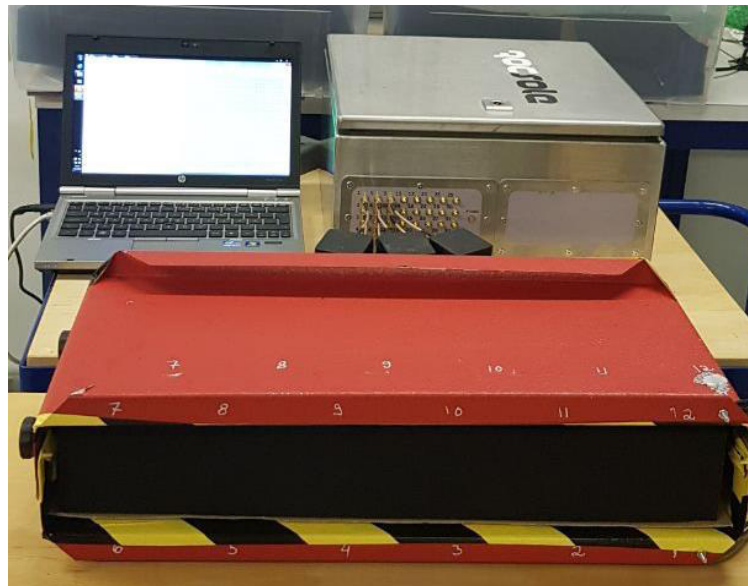


Figure 9: ECT sensor and the tomography device

As seen in Fig. 9, a board of an impregnated foam is placed inside the sensor. The 12 electrodes of this sensor are numbered on the front surface. The tomography device applies voltages to these electrodes and measures the enter-electrode capacitances. The measured data is sent to the connected laptop. For this experiment, three pieces of foam are cut from the foam board, moisturized and returned to their original location. Fig. 10 shows the removed pieces of foam.



<b>TOMOCON</b>				<b>GRANT AGREEMENT No.: 764902</b>	
Deliverable Title: <b>Experimental Validation Data of Improved Multiphysics Modelling</b>					
<b>Del. Rel. No.</b>	<b>EU Del. No.</b>	<b>WP No.</b>	<b>Lead Beneficiary</b>	<b>Type</b>	<b>Date</b>
D2.3.	D7	WP2	INPT / UEF	Report	25.02.2020



Figure 10: Experiment with ECT sensor by cutting three pieces of foam

After collecting the measured capacitances, the difference imaging technique as the reconstruction algorithm is used to estimate the difference of the target permittivity to the permittivity of the reference dry foam. The results of the reconstruction are shown in Fig. 11. As seen in this figure, the locations of the wet pieces are correctly identified in the reconstructed image by higher permittivity areas.

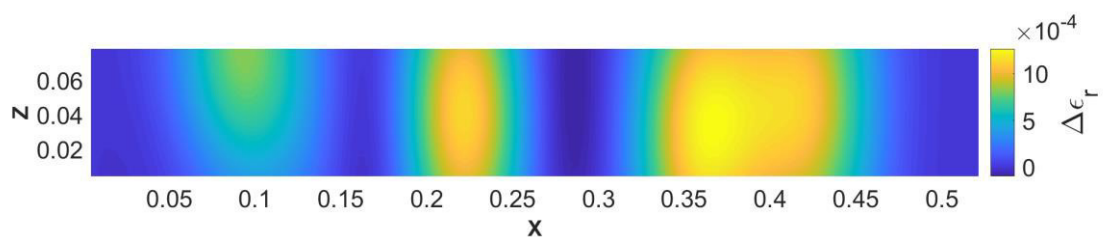


Figure 11: Reconstructed permittivity distribution

## 2.4 Microwave tomography

### 2.4.1 Measurement set-up

A microwave tomography measurement set-up is illustrated in Fig. 12. X-band (8.2-12.4 GHz) horn antennas are used to transmitting / receiving the electromagnetic signals. This kind of antenna is chosen to suppress the electromagnetic interferences from the high power device oven. The reflected electromagnetic waves from the foam with the cross-section of 50 cm × 7.6 cm, are measured with the vector network analyzer (VNA) and stored in a matrix. The different scattered fields corresponding to the various moisture levels are depicted in Fig. 13.



TOMOCON			GRANT AGREEMENT No.: 764902		
Deliverable Title: <b>Experimental Validation Data of Improved Multiphysics Modelling</b>					
Del. Rel. No.	EU Del. No.	WP No.	Lead Beneficiary	Type	Date
D2.3.	D7	WP2	INPT / UEF	Report	25.02.2020

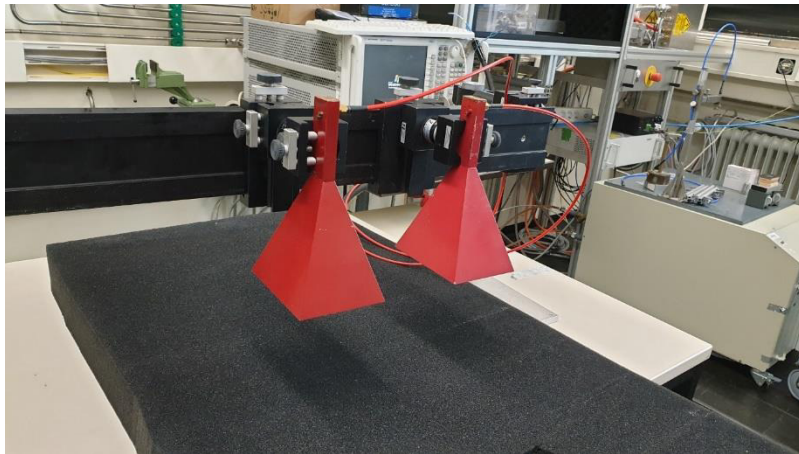


Figure 12: Microwave tomography measurement set-up

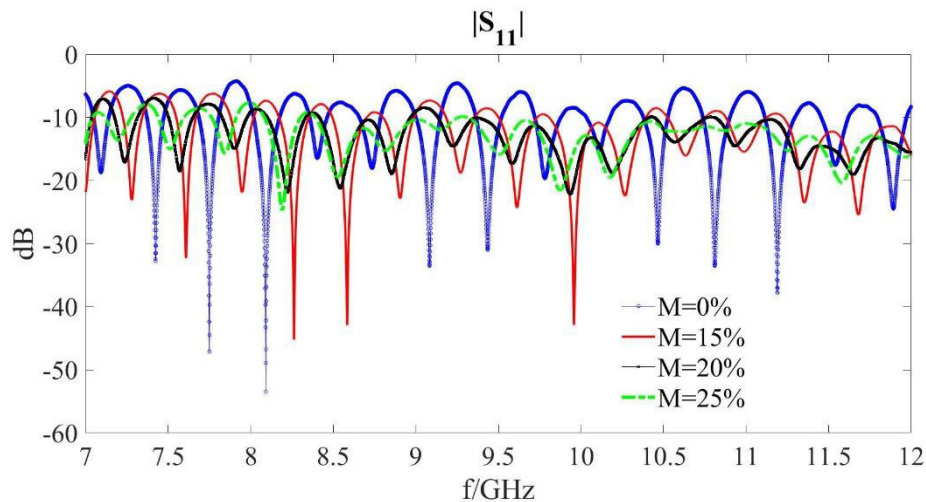


Figure 13: Return loss corresponding to different moisture levels

## 2.4.2 Reconstruction scheme

A fast (and accurate) reconstruction from MWT will provide enough reaction time for the control system to achieve selective heating in the drying process. Therefore, a neural network based approach is applied to meet the targeted time of less than a second for estimating the moisture content distribution. The feasibility of this approach is tested with synthetic measurement data first.

A convolutional neural network was trained using 15000 training samples to map the scattered fields to moisture distribution inside the foam. Assuming a smooth variation of moisture inside the foam, the moisture samples for the training and test dataset were generated using anisotropic Gaussian smoothness prior. The corresponding scattered fields for each moisture samples were measured from a numerically simulated MWT model with 11 dipole antennas. All measurements are performed at a 3 GHz frequency. The estimation results from the trained neural network are obtained in less than a second. Results for two example cases with low and moderate moisture content are shown in Fig. 14.



<b>TOMOCON</b>				<b>GRANT AGREEMENT No.: 764902</b>	
Deliverable Title: <b>Experimental Validation Data of Improved Multiphysics Modelling</b>					
<b>Del. Rel. No.</b>	<b>EU Del. No.</b>	<b>WP No.</b>	<b>Lead Beneficiary</b>	<b>Type</b>	<b>Date</b>
D2.3.	D7	WP2	INPT / UEF	Report	25.02.2020

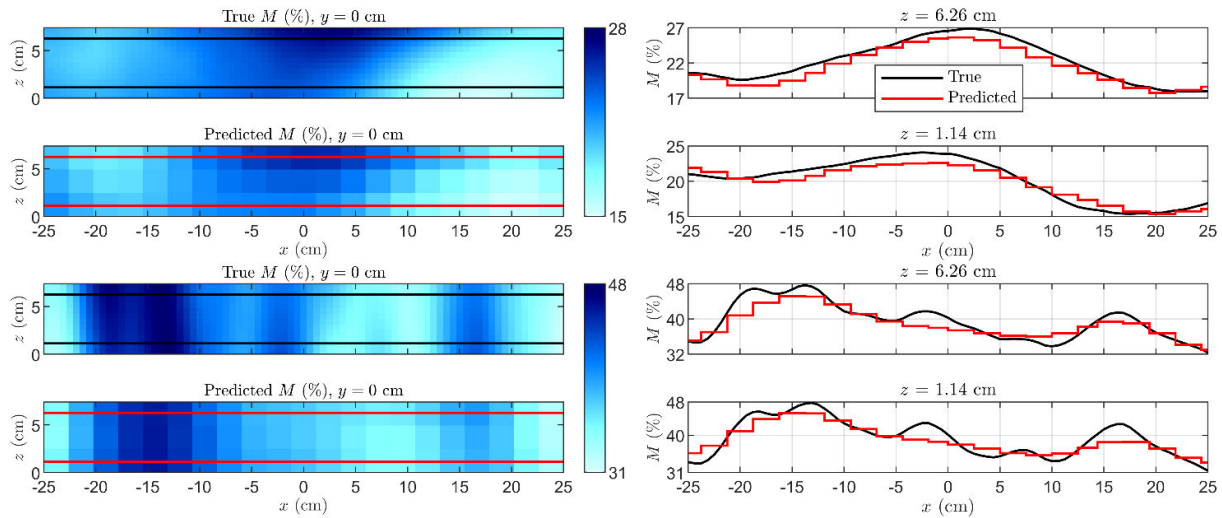


Figure 14: Two example cases having low (top) and moderate (bottom) moisture content. Pictures on the left show the true and predicted field values and pictures on the right for two fixed  $z$  values, respectively. The selected lines are visualized with black and red horizontal lines on the corresponding field graphs.

## 2.5 Human-Computer Interaction

Color coding is a fundamental technique for mapping data to visual representations, allowing users to carry out perception-based tasks. Following WP 5.2., we conducted the automatic segmentation in MWT images to understand and visualise the low moisture areas of foams after the confined microwave drying process. Thus, we intend to study how well color maps can support the visual comprehension of our tomographic image, more specifically, to investigate which color map(s) perform brilliantly in segmenting tomographic images both in human perception and in subjectivity in our microwave drying case. We conducted a crowdsourcing study of 11 different color schemes, as shown in Fig. 15 and Fig. 16.

Colormap	Description
'original'	Default colormap in MATLAB
viridis	Perceptually uniform sequential colormaps
plasma	
inferno	
magma	
cividis	
greys	Sequential colormap
cool	Sequential (2) colormaps
hot	
gist_heat	
copper	

Figure 15: The details of 11 color maps used



TOMOCON				GRANT AGREEMENT No.: 764902		
Deliverable Title: <b>Experimental Validation Data of Improved Multiphysics Modelling</b>						
Del. Rel. No.	EU Del. No.	WP No.	Lead Beneficiary	Type	Date	
D2.3.	D7	WP2	INPT / UEF	Report	25.02.2020	

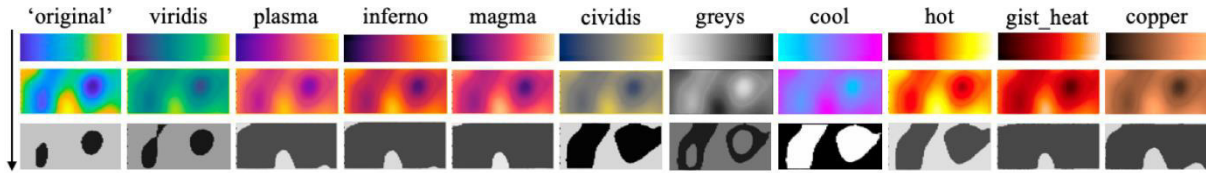


Figure 16: Each of the 11 color maps (1<sup>st</sup> row) is applied to the same MWT image sample resulting in (2<sup>nd</sup> row), and yielding segmented images (3<sup>rd</sup> row).

Over 40 participants were recruited to finish the user study so as to see the performance of every color map. Moreover, a quantitative evaluation of the schemes was employed. Based on the intersection of subjective and quantitative output, we infer that for the perception-based segmentation scientific analysis for MWT, we recommend the color maps hot and cool as the most suitable color schemes. For the same context of use, we do not suggest either magma or gist\_heat schemes as illustrated in Fig. 17.

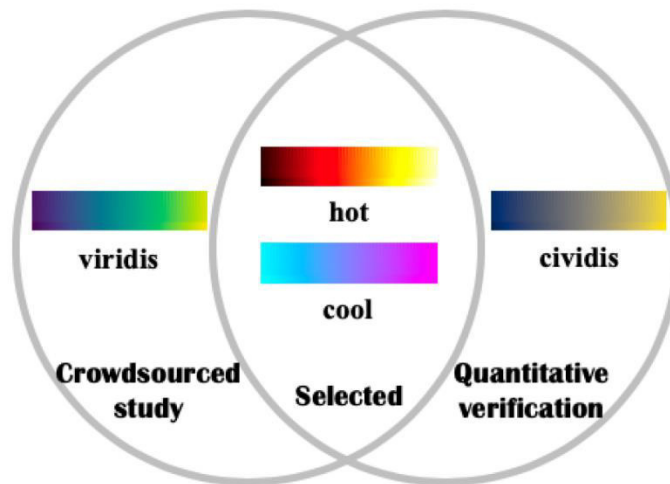


Figure 17: Intersection between crowdsourced study and quantitative verification

<b>TOMOCON</b>				<b>GRANT AGREEMENT No.: 764902</b>	
Deliverable Title: <b>Experimental Validation Data of Improved Multiphysics Modelling</b>					
<b>Del. Rel. No.</b>	<b>EU Del. No.</b>	<b>WP No.</b>	<b>Lead Beneficiary</b>	<b>Type</b>	<b>Date</b>
D2.3.	D7	WP2	INPT / UEF	Report	25.02.2020

### 3 Experimental data for code validation liquid metal flow (continuous casting)

#### 3.1 Experimental data from the HZDR Mini-LIMMCAST facility

##### 3.1.1 Description of the experimental facility

Experimental data needed for the validation of the numerical magnetohydrodynamic models of the liquid metal flow are gathered from the HZDR Mini-LIMMCAST facility. Mini-LIMMCAST is a hydrodynamically scaled laboratory model of the mold and strand of an industrial caster. It is operated as a continuous cold liquid metal loop using the eutectic alloy of Gallium-Indium-Tin (GaInSn). GaInSn is opaque, non-toxic, and liquid at room temperature and is used as a model of liquid steel. The schematic of the Mini-LIMMCAST is given in Figure 18. Liquid metal, initially stored in the catchment vessel is pumped to the tundish which acts as a buffer storage. The flow out of the tundish, through the submerged entry nozzle (SEN), and into the acrylic mold is regulated by the opening position of the stopper rod. The level in the mold is kept constant and adjusted by the position of the overflow dam, any overflowing metal is returned to the catchment tank.

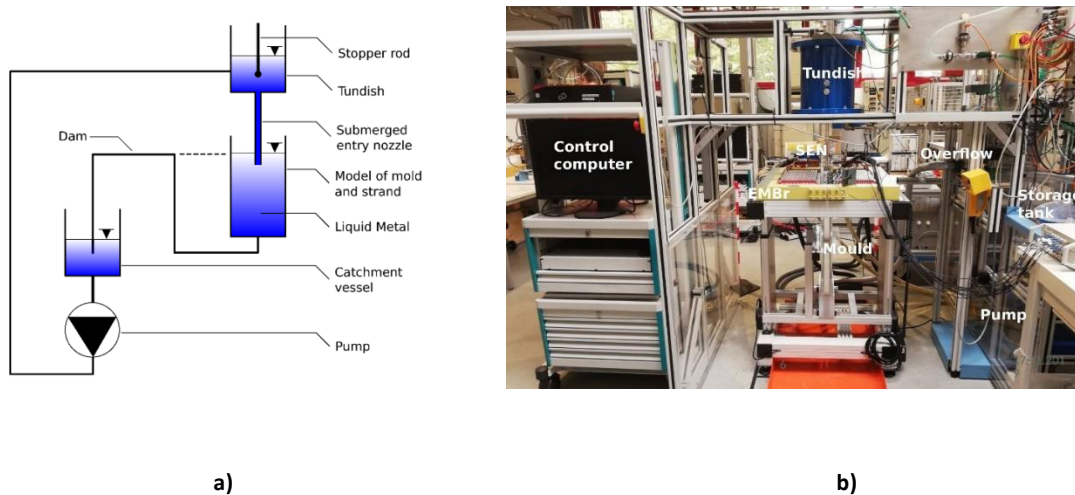


Figure 18: a) Schematic representation of the liquid metal loop (Schurmann et al., 2019); b) Photograph of the Mini-LIMMCAST

The mold and SEN are made out of acrylic glass. The mold dimension is 300 x 35 mm, The SEN has an inner diameter of 12 mm with two side ports directed downward at an angle of 15° (see Figure 19). Mini-LIMMCAST can be equipped with an electromagnetic brake that generates a static magnetic field at a defined vertical position along the entire width of the mold. It consists of two water cooled coils, which are connected in series, and the maximum magnetic field of 406 mT is generated using a current of 600 A. The vertical position of the EMBr can be precisely adjusted by a motorized system. Additionally, Mini-LIMMCAST will be equipped with Argon gas injection in order to achieve two-phase flow. Argon injection can be from the tip of the stopper rod, which is already manufactured and will be mounted at the facility in the next weeks. Additionally, gas can be injected through the side of the SEN.

##### 3.1.2 Measurement techniques

Two measurement techniques are being used to record the state of the experiment, Ultrasound Doppler Velocimetry (UDV) and Contactless Inductive Flow Tomography (CIFT). UDV measures the velocity components in the direction of the individual ultrasound beam along the entire length of the beam. Multiple sensors can be arranged in an array to get the 2D representation of the flow in the measurement plane. Figure 20 shows the 2D image of the flow in horizontal direction recorded with 10 ultrasound sensors using UDV.



TOMOCON			GRANT AGREEMENT No.: 764902		
Deliverable Title: <b>Experimental Validation Data of Improved Multiphysics Modelling</b>					
Del. Rel. No.	EU Del. No.	WP No.	Lead Beneficiary	Type	Date
D2.3.	D7	WP2	INPT / UEF	Report	25.02.2020

UDV is a well-established measurement technique that can reliably be used to validate the numerical models, since it has a high spatial as well as temporal resolution. By changing the strength of the magnetic field or the position of the magnetic field it is possible to cover large parameter space to gather sufficient information for successful validation. Schurmann et al. (2019) published an extensive study, performed on the Mini-LIMMCAST facility, of electromagnetic field influence on the liquid metal flow for different strengths and positions of the magnetic field. Additionally, four specific cases have been selected to compare directly with numerical simulations, for the magnetic field strength of 0 mT, 100 mT, 200 mT, and 300 mT, while the position of the magnetic field is kept constant, i.e. the center of the EMBr is at 78 mm below the free surface (see Figure 19). Measurement records data with a time resolution of 3 frames per second. Data from measurements are exported to VTK files. The origin of the coordinate system is exactly the same as used in the numerical simulation, so that a comparison can be done without further post processing.

CIFT is used to measure the perturbations of the magnetic field caused by the flow of the conductive liquid metal, this is *flow induced magnetic field*. The AC magnetic field with about 1 Hz and an amplitude in an order of 1,5 mT is generated by the two rectangular coils. The magnetic field is measured by gradiometric pick-up coils. The voltage induced in the coils is proportional to the change of the AC excitation magnetic field and its perturbations caused by the flow of liquid metal. The resulting measurement of voltage is then phase separated in the excitation field component and the flow induced field component using quadrature demodulation. The sampling time of the flow induced magnetic field resulted from quadrature demodulation is inherently limited by the excitation frequency and in our case a sample is generated once every second. Further, by resolving the linear inverse problem, it is possible to get the reconstruction of the fluid flow inside the mold. The reconstructed flow is also saved in VTK files similar to the UDV measurements.

Additional measurement techniques for bubble detection will be implemented. For the detection of the gas distribution in the SEN, mutual inductance tomography (MIT) will be used. For each reconstruction the distribution of the gas in the SEN will be saved as a scalar matrix in MATLAB's ".mat" file, and additionally as a ".csv" file. The voltage measurement from the MIT coils is saved as a ".csv" file.

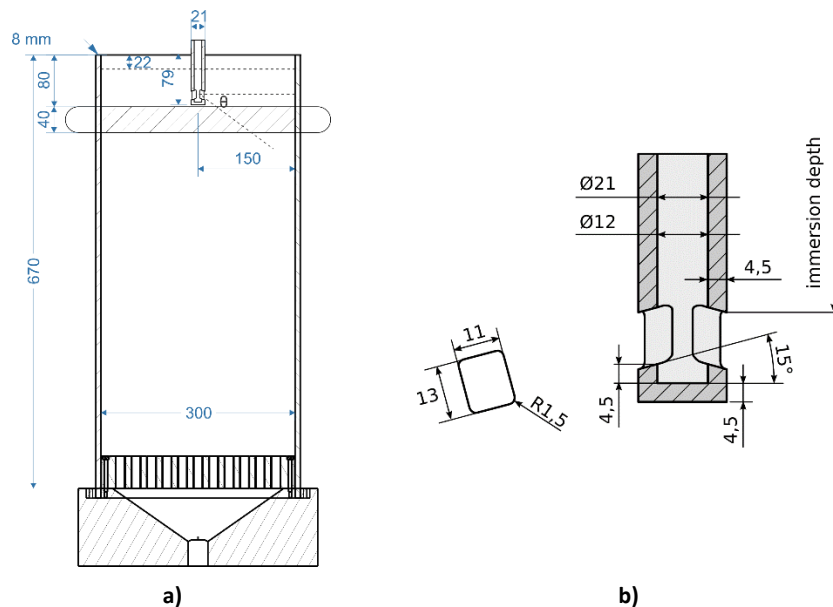


Figure 19: a) Mold drawing; b) SEN drawing



TOMOCON				GRANT AGREEMENT No.: 764902	
Deliverable Title: <b>Experimental Validation Data of Improved Multiphysics Modelling</b>					
Del. Rel. No.	EU Del. No.	WP No.	Lead Beneficiary	Type	Date
D2.3.	D7	WP2	INPT / UEF	Report	25.02.2020

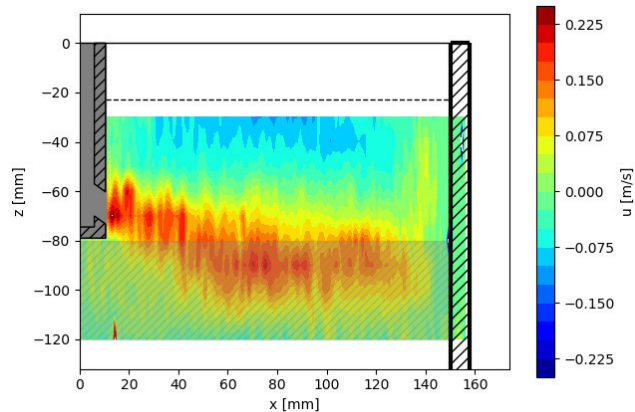


Figure 20: Velocity profile recorded using UDV

As a different method, a sensor built from 64 resistive probes is foreseen. It will allow the detection of the special bubble distribution in one cross section of the mold. The data format of this new technique will be defined later.

Additionally, CIFT measurements were done without flow and with a change of strength of the magnetic field. The measurement campaign was done for calibration purposes, in order to further study the effect of the strong magnetic field on the sensitivity of the CIFT measurement. A series of measurements where the strength of the brake was changed both in linear and in pseudorandom order was conducted to study the codependence. Figure 21 shows how the measured flow induced magnetic field depends on the strong magnetic field of the EMBr.

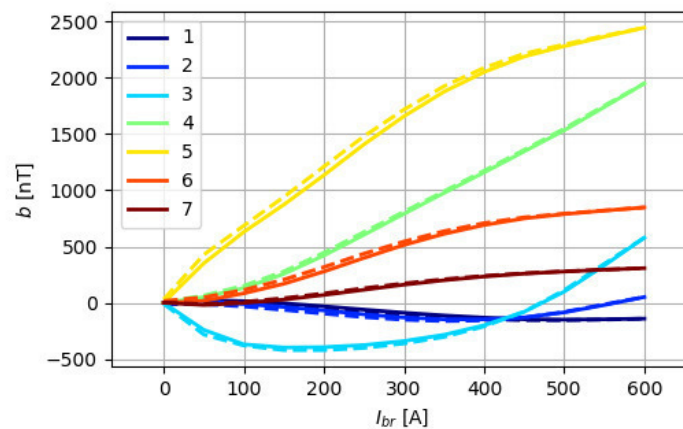


Figure 21: Effect of the strong magnetic field on the CIFT measurement

### 3.1.3 Data formats and repository

UDV data is stored in devices native binary files. Each file, one for every measurement, contains information of the fluid velocity at a distance from the sensor for each sensor, for every timestep. Additionally, measurements from UDV are converted to the “VTK” format for easier visualization and comparison. The origin of the coordinate system matches the one used in the numerical simulations.

The CIFT measurements of the voltage induced in the pickup coils are stored in “.csv” files for each measurement timestep for all sensors. The final reconstruction is saved in a “.dat” for each reconstruction frame. The “.dat” file has all three velocity components  $v_x$ ,  $v_y$ , and  $v_z$  the coordinates of the point for which velocities are stored are stored in a separate “.dat” file. Additionally, the reconstructed velocity will be saved in VTK files, where the origin of the coordinate system is equal to the one used in the numerical simulations.



<b>TOMOCON</b>			<b>GRANT AGREEMENT No.: 764902</b>		
Deliverable Title: <b>Experimental Validation Data of Improved Multiphysics Modelling</b>					
<b>Del. Rel. No.</b>	<b>EU Del. No.</b>	<b>WP No.</b>	<b>Lead Beneficiary</b>	<b>Type</b>	<b>Date</b>
D2.3.	D7	WP2	INPT / UEF	Report	25.02.2020

The MIT voltage measurements are saved in a “.csv” file, and the reconstructed images are saved as a scalar matrix in a binary MATLAB “.mat” file.

All valid measurement data, and data needed for multiphysics modeling is stored on HZDR's *OwnCloud* platform forming dedicated folders for measurement techniques, with a subfolder structure that denotes the date of the recorded measurement (e.g. folder name: *YYYYMMDD*). Every measurement campaign must include additional metadata that describes the experimental conditions.



<b>TOMOCON</b>			<b>GRANT AGREEMENT No.: 764902</b>		
Deliverable Title: <b>Experimental Validation Data of Improved Multiphysics Modelling</b>					
<b>Del. Rel. No.</b>	<b>EU Del. No.</b>	<b>WP No.</b>	<b>Lead Beneficiary</b>	<b>Type</b>	<b>Date</b>
D2.3.	D7	WP2	INPT / UEF	Report	25.02.2020

## 4 Experimental data for code validation of particle formation in semibatch crystallization process

### 4.1 Experimental data from LUT continuous carbon capture and crystallization units

#### 4.1.1 Description of the experimental facility

The system under investigation is a semibatch reaction type crystallization process of calcium carbonate working based on dissolving high-pH carbonated water in a calcium chloride ( $\text{CaCl}_2$ ) solution. Following the TOMOCON Deliverable 5.2 (29.09.2019 - EU Del. No. 16), the crystallization process is integrated with a continuously operated carbon dioxide ( $\text{CO}_2$ ) capture unit, which runs based on a highly alkaline absorbent solution and membrane contactor. The  $\text{CO}_2$  capture unit consists of a hollow fiber membrane module (3M Liqui-Cel™ polypropylene hollow-fiber) as the absorber, a glass vessel that acts as a stripper, and a buffer tank for the absorbent solution (Nieminen et al., 2020). Figure 22 shows the overall flowsheet of the process that leads to the production of solid calcium carbonate particles.

A small-scale laboratory reactor ( $V=0.5$  L) equipped with a magnetic stirrer is used to conduct the crystallization process and to obtain the micron-sized precipitated material. A photograph of the carbon dioxide capture unit and small-scale crystallization operation is displayed in Figure 23a and 23b, respectively. A reactor with a diameter of 30 cm (Height/Diameter=1) is under construction at the LUT University, which will be studied for the process scale-up starting from May 2020. The electrical and ultrasound tomographic sensors are planned to be assembled in a circular arrangement around the newly built reactor later in the year 2020 during the secondments of ESRs 11 and 13 in Lappeenranta, Finland.

The materials used to conduct the experiments include calcium chloride dried powder ( $\text{CaCl}_2$ , purity  $\geq 96\%$ , Merck), sodium hydroxide 1 Molar ( $\text{NaOH}$ , purity  $\geq 99\%$ , VWR) for pH control. Buffer solutions (Mettler Toledo) with pH of 4.00, 7.00 and 10.00 were utilized to calibrate an in-situ pH meter (Consort C3010). The addition rate of the reagent to the crystallizer is controlled by a Masterflex L/S syringe pump ( $d = 3.83$  mm). The total  $\text{CO}_2$  content of the liquid samples after the carbonation process was determined by titration with 1 molar hydrochloric acid ( $\text{HCl}$ ) using a specifically designed Chittick-apparatus (Soham Scientific) (Figure 23c).

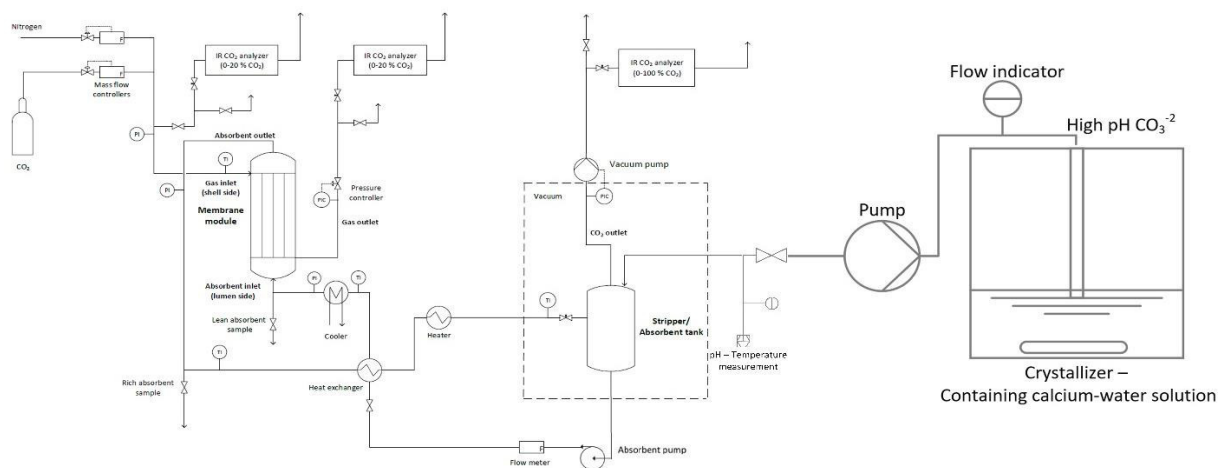


Fig. 22: Flowsheet of the integrated  $\text{CO}_2$  capture unit and crystallization process of micron-sized  $\text{CaCO}_3$



TOMOCON				GRANT AGREEMENT No.: 764902	
Deliverable Title: <b>Experimental Validation Data of Improved Multiphysics Modelling</b>					
Del. Rel. No.	EU Del. No.	WP No.	Lead Beneficiary	Type	Date
D2.3.	D7	WP2	INPT / UEF	Report	25.02.2020

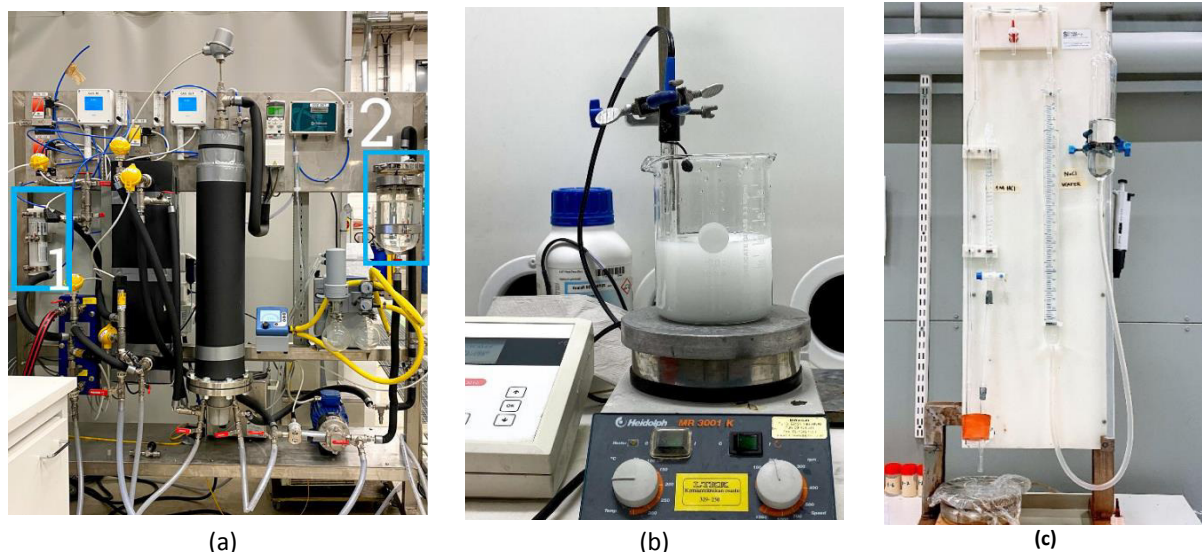


Fig. 13: (a) Photograph of the CO<sub>2</sub> capture unit: 1. Membrane contactor and 2. CO<sub>2</sub>-loaded solution; (b) Small-scale crystallizer equipped with a magnetic stirrer with online pH measurement; (c) Chittick-apparatus for determining CO<sub>2</sub> content in the absorbent solution.

#### 4.1.2 Measurement techniques

After each set of experiment, solid particles were immediately filtered from the mother solution by vacuum filtration and dried in an oven for 2 hours at 70°C. The particle size distribution (PSD) of the final product from each semibatch operation was measured by the laser diffraction method in a particle size analyzer. The identical amounts of sample from each experiment were used for this purpose. Each measurement is repeated for a total of 5 times and the averaged result for volume mean diameter and PSD is reported.

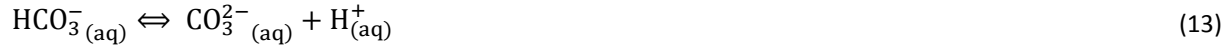
The electrical resistance tomography (ERT) device, which is currently under development, is equipped with 16 electrodes. A constant voltage is injected through one electrode and currents are measured simultaneously using the remaining 15 electrodes. The frequency of operation is 156 KHz and the image capturing frame rate is 2 Hz. Moreover, the proposed ultrasound computed tomography (USCT) system can be divided into three basic components: An array of multi-piezoelectric sensors, a sensing electronics setup for data acquisition and a computer system for image reconstruction. This system consists of a ring of 32 piezoelectric transducers operating at a frequency of 200 KHz. It is expected that these devices and sensors evaluate the differences in the solid density inside the reactor during the crystallization process. The denser regions within the reactor would have a different conductivity as compared to the regions with lesser density. Along with this, the suspension height would be measured vertically. The solid suspension height could be proportional to the average particle size through settling velocity, suspension density or final yield.

#### 4.1.3 Description of the experiment

The chemical absorbent selected for the current process is a highly alkaline water solution at atmospheric pressure. Solutions of carbonate ions were prepared by a continuous carbon capture process using high-pH distilled water as the absorbent. Gaseous carbon dioxide has several transformations upon its dissolution in water. The chemical system that describes the speciation of CO<sub>2</sub> in natural water is well-established and can be represented according to the following sequence of reactions,



<b>TOMOCON</b>				<b>GRANT AGREEMENT No.: 764902</b>	
Deliverable Title: <b>Experimental Validation Data of Improved Multiphysics Modelling</b>					
<b>Del. Rel. No.</b>	<b>EU Del. No.</b>	<b>WP No.</b>	<b>Lead Beneficiary</b>	<b>Type</b>	<b>Date</b>
D2.3.	D7	WP2	INPT / UEF	Report	25.02.2020



In atmospheric pressure (1 atm, 101325 Pa) and ambient temperature (20–25 °C), carbon dioxide is scarcely soluble in water (0.0384 mol/l at 20 °C) (Dean, 1999). The CO<sub>2</sub> absorption is enhanced by increasing the alkalinity of the solution, and since pH significantly modifies the amount of ionic species present in the aqueous solution, hence, certain carbonate concentrations could be achieved by controlling the pH of water for the carbon dioxide dissolution. Therefore, to increase the absorption amount of CO<sub>2</sub> in deionized water and to achieve a certain carbonate concentration, different hydroxide (OH<sup>-</sup>) concentrations were considered. Figure 24 shows the total CO<sub>2</sub> content at different initial concentrations of the absorbent solution. The total CO<sub>2</sub> content of the liquid samples after the carbonation process is determined by the titration method using the Chittick apparatus and subsequently evaluated using the ideal gas law as follows (Norouzbahari et al., 2016),

$$\alpha_{\text{CO}_2} = \frac{\text{mol}_{\text{CO}_2}}{\text{mol}_{\text{OH}^-}} = \frac{\left[ \frac{(V_{\text{gas}} - V_{\text{HCl}})(P)}{RT} \right]}{C_1 V_1} \quad (14)$$

where,  $V_{\text{gas}}$  (ml) denotes the volume of the displaced liquid in the graduated gas measuring tube of the titration instrument,  $R$  is the universal gas constant equal to 8.314 (j/mol-k),  $P$  (kPa) and  $T$  (K) represent the atmospheric pressure (101.325 kPa) and the ambient temperature, respectively. The volume of the released CO<sub>2</sub> gas is obtained after subtracting the HCl solution volume added to the Erlenmeyer flask,  $V_{\text{HCl}}$  (ml) from  $V_{\text{gas}}$ , as follows,

$$V_{\text{CO}_2} = V_{\text{gas}} - V_{\text{HCl}} \quad (15)$$

Additionally,  $C_1$  (mol.l<sup>-1</sup>) and  $V_1$  (ml) stand for the aqueous absorbent solution concentration and the liquid sample volume, respectively. Figure 25 represents the performance of the membrane module in absorbing carbon dioxide at various initial hydroxide concentrations.

After obtaining the CO<sub>2</sub>-rich solution, crystallization experiments can be carried out based on the following chemical reaction,

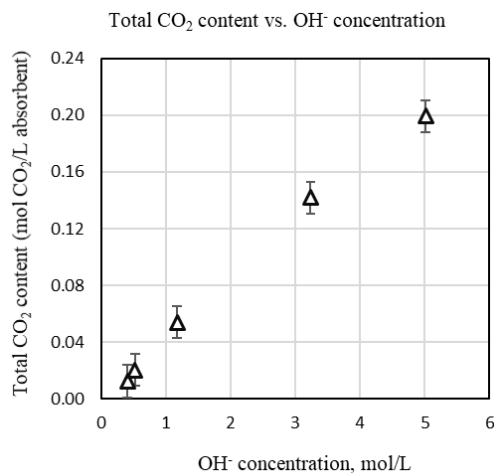
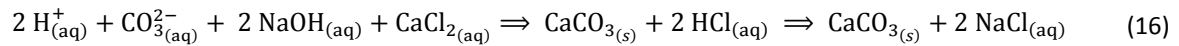


**Fig. 24: Total CO<sub>2</sub> content at different initial concentrations of the absorbent solution**

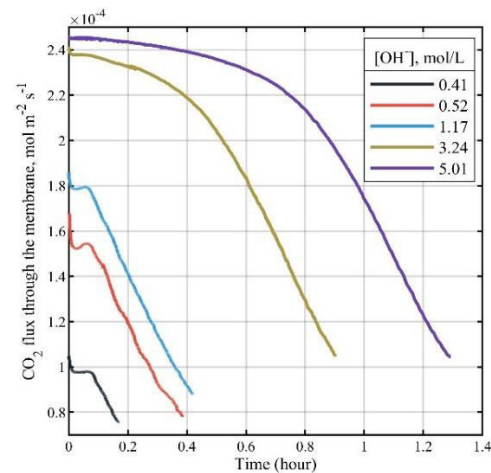


**Fig. 25: Carbon dioxide absorption performance of the membrane module based on initial pH**

where the feed solution consists of a high pH CO<sub>3</sub><sup>2-</sup> ions and the receiving reactor contains calcium ions. Throughout this fast-chemical reaction, micron-sized particles of CaCO<sub>3</sub>, which at first appear as cloudiness in



TOMOCON				GRANT AGREEMENT No.: 764902	
Deliverable Title: <b>Experimental Validation Data of Improved Multiphysics Modelling</b>					
Del. Rel. No.	EU Del. No.	WP No.	Lead Beneficiary	Type	Date
D2.3.	D7	WP2	INPT / UEF	Report	25.02.2020

the suspension, settle to the bottom of the crystallizer. For each semibatch operation, a constant concentration of a 300 g/L CaCl<sub>2</sub> solution was prepared in deionized water. The initial crystallizer volume containing excess amounts of calcium ions throughout each semibatch process was 0.1 l. Since the CaCl<sub>2</sub> dissolution in water is exothermic, the temperature of the solution was monitored with a thermostat to reach the stable working temperature of 21±2 °C.

In a reaction type crystallization technique, the temporal and spatial degree of homogeneity within the crystallizer is sensitive to agitation conditions. Accordingly, crystallization experiments were carried out at three different mixing speeds of 50, 300 and 600 RPM and four different flow rates of 1, 2.5, 5 and 10 ml/min to investigate these effects on volume mean particle diameter (also called the DeBroukere mean,  $d_{43}$ ) and particle size distribution (PSD). As displayed in Figure 26, it can be seen that higher mixing speeds promote particles bigger in mean diameter. This is because a higher stirring rate favors the growth phenomenon and generates an environment where supersaturation gets uniformly distributed at micro, meso and macro scales. This is also illustrated in the form of size distribution curves in Figure 27, where distribution is to a certain extent broader at lower feed rates.

The ongoing multiphysics simulations will be validated against the acquired  $d_{43}$  and PSD by coupling the species transport equation with the discrete method of population balance equation (PBE) in the ANSYS Fluent CFD code.

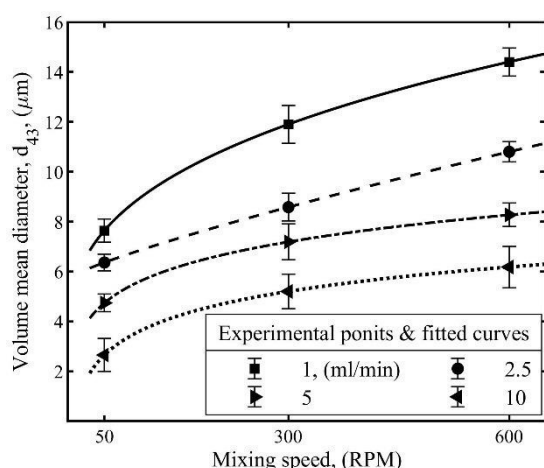


**Fig. 26: Effect of mixing speed at multiple feed rates on average diameter of CaCO<sub>3</sub> particles with associated error bars**

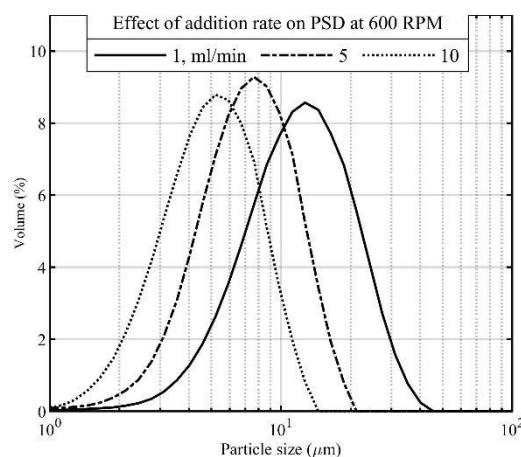


**Fig. 27: CaCO<sub>3</sub> particle size distribution at three different addition rates at a mixing speed of 600 RPM**

#### 4.1.4 Data formats and repository

Experimental measurements and characterization data are obtained from multiple online and offline instruments as follows,

- Particle size analyzer Mastersizer 3000 (Malvern Instruments, UK),
- Crystal lattice analysis (Bruker D8 Advance X-ray diffractometer),
- Continuous pH Meter (Consort C3010),
- Continuous carbon capture unit,
- Scanning electron microscope (SEM SU 3500 Hitachi),
- Electrical / Ultrasound tomographic sensors.

Thus, a post processing is required to make the raw formats easily available. Experimental measurements are sorted and categorized by the date of the experiment and contain all the files related to that process. A “readme.txt” file is included in each folder that provides an overview of each experiment. Additionally, the documentation of instruments, equipment, accompanied literature researches and published papers are also in-



<b>TOMOCON</b>				<b>GRANT AGREEMENT No.: 764902</b>	
Deliverable Title: <b>Experimental Validation Data of Improved Multiphysics Modelling</b>					
<b>Del. Rel. No.</b>	<b>EU Del. No.</b>	<b>WP No.</b>	<b>Lead Beneficiary</b>	<b>Type</b>	<b>Date</b>
D2.3.	D7	WP2	INPT / UEF	Report	25.02.2020

cluded in the repository. All these materials are stored in LUT University's OneDrive-based workspace and a Google Drive online storage that is shared between the partners.

Numeric results from the experiments are stored in Excel Workbook file format (\*.xlsx) and sorted in column vector mode. Additionally, these data are stored as MATLAB®-exclusive MAT-file with associated \*.m file scripts for generating the necessary plots and figures. MATLAB® m-file scripts are optimized to create publication-quality figures based on Encapsulated PostScript (\*.eps) file format that can be used in LaTeX projects as well. A summary of the file formats that have been used and processed during the experimental works are tabulated in Table 2.

**Table 2: Summary of the file formats generated from various measuring instruments during a full crystallization process cycle**

#	Measuring instrument	Raw format	.xlsx Workbook	.mat File	.m script ready	Type of measurement	Comment
1	Particle size analyzer	.csv, .mmes	<input checked="" type="checkbox"/>	<input checked="" type="checkbox"/>	<input checked="" type="checkbox"/>	Offline	Generates $d_{43}$ and PSD. The analyzer working file format is .mmes.
2	X-ray diffractometer	.brml, .eva, .csv	<input checked="" type="checkbox"/>	<input checked="" type="checkbox"/>	<input checked="" type="checkbox"/>	Offline	.brml, .eva are output results of X-Ray unit.
3	pH Meter	.txt, .csv	<input checked="" type="checkbox"/>	<input checked="" type="checkbox"/>	<input checked="" type="checkbox"/>	Real-time & Online	PH sensor is calibrated each time before beginning the measurements.
4	CO <sub>2</sub> unit	.lvm	<input type="checkbox"/>	<input checked="" type="checkbox"/>	<input checked="" type="checkbox"/>	Real-time & Online	Based on the LabVIEW software measurement file format.
5	SEM	.tif	<input type="checkbox"/>	<input type="checkbox"/>	<input type="checkbox"/>	Offline	High quality scanning electron microscope images.
6	Process schematics	.vsdx	<input type="checkbox"/>	<input type="checkbox"/>	<input type="checkbox"/>	N/A	Microsoft Visio software (LUT University license) file format for creating detailed process schematics.
7	Tomographic sensors	.tif, .jpeg	<input type="checkbox"/>	<input type="checkbox"/>	<input type="checkbox"/>	Real-time & Online	Output format of the tomographic measurements (Requires update after full implementation).



TOMOCON			GRANT AGREEMENT No.: 764902		
Deliverable Title: <b>Experimental Validation Data of Improved Multiphysics Modelling</b>					
<b>Del. Rel. No.</b>	<b>EU Del. No.</b>	<b>WP No.</b>	<b>Lead Beneficiary</b>	<b>Type</b>	<b>Date</b>
D2.3.	D7	WP2	INPT / UEF	Report	25.02.2020

## 5 Experimental data for the saturated sucrose solution and crystals observation

### 5.1 Experimental data from Process tomography laboratory at Technical University of Lodz

#### 5.1.1 Description of the Electrical Resistance Tomography (ERT) experimental facility

The experiments were performed at the Process Tomography Laboratory at Lodz University of Technology, Poland. Various reactors were designed with a diameter of 90 mm and 300 mm. A single plane of ERT sensor was mounted on these reactors. The detailed image of reactor is shown in Figures 28 (a) -2. The double plane mounted reactor is also shown in Figure 28 (b) -9. The experiments were conducted using the electrical tomography system developed at the Research and Development facility of ROCSOLE Ltd Finland. Advanced transformers were used to detect the low conductivity solutions. These transformers have the signal conditioning unit inbuilt inside which assures a good signal to the noise ratio and specialized co-axial cables for lossless data transmission. The phantoms were printed using the Ultimaker 3E 3D-printer using the ABS as the printing material.

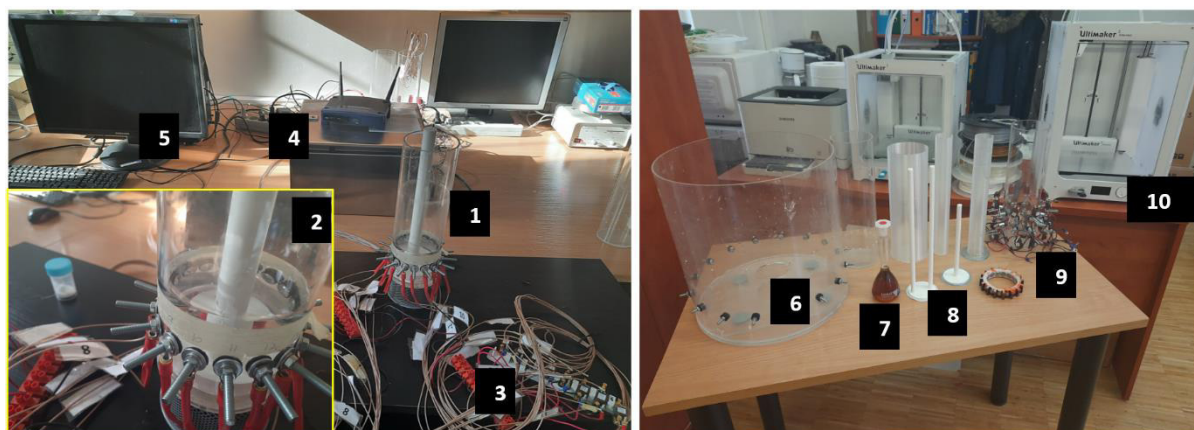


Figure 28: Tom Dyakowski Process Tomography Laboratory (a) 1: 90 mm reactor, 2: 16 x 1 plane sensors mounted, 3: Advanced transformers for low level conductivity measurement, 4: Rocsole ERT device and router for wireless connectivity, 5: Stand-alone computer for data acquisition and storage using Tomokis Software  
(b) 6: 300 mm reactor, 7: Sample saturated sucrose solution, 8: 3D printed Phantoms for measurement, 9: 8 x 2 plane sensors mounted, 10: Ultimaker 3 Extended 3D printer

The phantoms of the sizes 10 mm, 10 mm x 2, 20 mm, 30 mm, 40 mm and 50 mm were printed. The saturated sucrose solution was obtained from the Polish sugar industry Polski Cukier. Three concentrations of the sucrose solution were evaluated using this solution.

Table 3: Sensor specifications

	Reactor 1	Reactor 2
<b>Diameter</b>	90 mm	300 mm
<b>Number of Layers</b>	1	1
<b>Number of Electrodes Per Layer</b>	16	16
<b>Electrodes Material</b>	Stainless Steel	Stainless Steel
<b>Head Size</b>	12 mm	12 mm
<b>Thread Size</b>	5 mm	5 mm
<b>Distance Between Each Electrode</b>	2.7 mm	58.875 mm



TOMOCON				GRANT AGREEMENT No.: 764902	
Deliverable Title: <b>Experimental Validation Data of Improved Multiphysics Modelling</b>					
Del. Rel. No.	EU Del. No.	WP No.	Lead Beneficiary	Type	Date
D2.3.	D7	WP2	INPT / UEF	Report	25.02.2020

### 5.1.2 Measurement techniques in ERT

There are many aqueous based solutions in which the ERT imaging methodology is suitable for analysis. Miscible liquids, non-miscible liquids, and solid-liquid mixing processes are some of the applications. ERT offers a complementary and a low cost substitute for the non-invasive monitoring of the processes [6]. For the experimental validation, the separation of the sugar crystals from the very low conductivity saturated sucrose solution was performed.

Conductivity (or specific conductance) of an electrolyte solution is a measure of its ability to conduct electricity. The SI unit of conductivity is Siemens per meter (S/m). It is inverse of the resistivity  $\rho$  which is given by equation 17:

$$R = \rho \frac{l}{A} \quad (17)$$

Here  $R$  is the resistance,  $l$  is the length between the two electrodes and  $A$  is the cross-sectional area of the sample. Electrical resistance tomography is a technique of electrical voltage or current injection and measuring the electrical field distribution to reconstruct a three-dimensional image using inverse imaging techniques. Figure 29 (a) shows a schematic of a voltage injected current measured (V-I) method of an ERT acquisition system, where a modified Bayesian technique is utilized for the image reconstruction. These reconstructed images provide the conductivity distribution in a planar view of the circular sensor. The conductivity distribution is proportional to the crystal formation or crystal growth in the planar region of interest. A targeted multi-planar ERT acquisition schematic is also illustrated in Figure 29 (b).

The physical relationship between the conductivity distribution inside the domain and the boundary voltages is governed by a partial differential equation derived from Maxwell equations [7].

$$\int_{el} \sigma \frac{\partial u}{\partial v} ds = -I_l \quad (18)$$

Where  $\sigma$  is the conductivity distribution,  $u$  is the electric potential, and  $el$  is the area of the electrode,  $v$  is the outward normal.  $I_l$  is the current injected through the electrode  $el$  on the surface  $ds$ . The ERT device, which is currently under development, is equipped with 16 electrodes; a constant voltage is injected through one electrode and currents are measured simultaneously using the remaining 15 electrodes. The test setup, as displayed in Figure 29 (c), demonstrates the placement of the electrodes and the signal processing unit mounted on every electrode. Figure 29 (d) shows the reconstructed images of a 10 mm diameter non-conductive phantom in water. To test the conductivity distribution, a saturated sucrose solution of 250 ml is prepared, and 100 g of white granulated sugar is released into this solution. More results for different phantoms and sucrose solutions were presented in our publication [8]. The solid crystals are observed in the reconstructed images. Figure 29 (e) shows a conductivity distribution of a very low conducting saturated solution with the presence of solid particles in black. The video of the sugar crystals movement has been attached in the repository (see section 5.1.3).

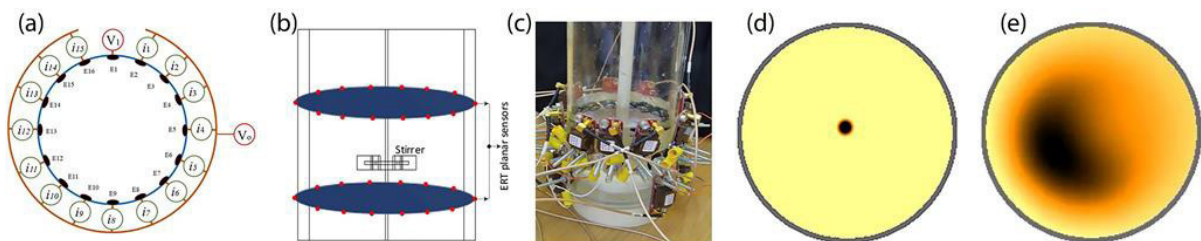


**Figure 29: Semibatch reactor equipped with multi sensor process monitoring; (a) V-I based ERT acquisition schematic; (b) Multi-planar monitoring of the calcium carbonate precipitation; (c) ERT electrodes around the test reactor; (d) Reconstruction of a test 10 mm phantom; (e) Preliminary results from sugar crystals distribution in a saturated sucrose solution**



<b>TOMOCON</b>			<b>GRANT AGREEMENT No.: 764902</b>		
Deliverable Title: <b>Experimental Validation Data of Improved Multiphysics Modelling</b>					
<b>Del. Rel. No.</b>	<b>EU Del. No.</b>	<b>WP No.</b>	<b>Lead Beneficiary</b>	<b>Type</b>	<b>Date</b>
D2.3.	D7	WP2	INPT / UEF	Report	25.02.2020

### 5.1.3 Data formats and repository

The data from the experimental campaign of TUL is uploaded on Onedrive and can be accessed using the following URL:

[https://tulodz-my.sharepoint.com/:f/g/personal/guruprasad\\_rao\\_p\\_lodz\\_pl/EjDBIAUFNY9Ehvgu\\_roDOXQBGD-GJfbZ6mft-AvDIOgKqtg?e=AcTYQA](https://tulodz-my.sharepoint.com/:f/g/personal/guruprasad_rao_p_lodz_pl/EjDBIAUFNY9Ehvgu_roDOXQBGD-GJfbZ6mft-AvDIOgKqtg?e=AcTYQA)

The data is stored in a folder, named as “ERT experimental validation”.

This folder contains three subfolders named as:

- ERT data: It consists of the ERT data in the zip format.
- Phantom Designs: Design of the phantoms in the blend format. Images of the proportional visualization of the phantoms in .tif format.
- Reconstructed Images: Images for the sample of 50 % of the saturation using G-N iterative reconstruction method.
- Video: It contains the video of the sugar crystals being added to the saturated sucrose solution.

The raw data in the ERT folder is stored in the “.zip” format. After extracting the files, all the details of the experiment would be extracted in a folder. We have to choose caps folder to get a “.txt” file. This file consists of the readings in a  $16 \times 16 = 256$  matrix format. These are resistance data and voltage data which would be utilized for the reconstruction purposes using EIDORS-Matlab.



<b>TOMOCON</b>				<b>GRANT AGREEMENT No.: 764902</b>	
Deliverable Title: <b>Experimental Validation Data of Improved Multiphysics Modelling</b>					
<b>Del. Rel. No.</b>	<b>EU Del. No.</b>	<b>WP No.</b>	<b>Lead Beneficiary</b>	<b>Type</b>	<b>Date</b>
D2.3.	D7	WP2	INPT / UEF	Report	25.02.2020

## 6 References

- [1] Slot, J. (2013), Development of a centrifugal inline separator for oil-water flows (Ph.D. dissertation). University of Twente, Enschede.
- [2] Schurmann, D., Glavinić, I., Willers, B., Timmel, K., and Eckert, S. (2019a), Impact of the electromagnetic brake position on the flow structure in a slab continuous casting mold: An experimental parameter study. *Metallurgical and Materials Transactions B*, DOI:10.1007/s11663-019-01721-x.
- [3] Dean, J.A. (1999), *Lange's Handbook of Chemistry*. New York; London: McGraw-Hill, Inc.
- [4] Nieminen, H., Järvinen, L., Ruuskanen, V., Laari, A., Koironen, T. and Ahola, J. (2020), Insights into a membrane contactor based demonstration unit for CO<sub>2</sub> capture. *Separation and Purification Technology*, Vol. 231, p. 115951.
- [5] Norouzbahari, S., Shahhosseini, S. and Ghaemi, A. (2016), Chemical absorption of CO<sub>2</sub> into an aqueous piperazine (PZ) solution: development and validation of a rigorous dynamic rate-based model. *RSC Adv.*, Vol. 6 No. 46, pp. 40017–40032.
- [6] Dickin, F. and Wang, M. (1996), Electrical resistance tomography for process applications. *Measurement Science and Technology*, Vol. 7, p. 247.
- [7] Kim, B. S., Khambampati, A. K., Jang, Y. J., Kim, K. Y. and Kim, S. (2014), Image reconstruction using voltage-current system in electrical impedance tomography. *Nuclear Engineering and Design*, Vol. 278, pp. 134-140.
- [8] Rao, G., Sattar, M. A., Wajman, R., Jackowska-Strumillo, L. (2019), Application of the 2D-ERT to evaluate phantom circumscribed regions in various sucrose solution concentrations. *International Interdisciplinary PhD Workshop (IIPHDW)*, 15–17th May 2019, Wismar, Germany, IEEE Xplore Digital Library, pp. 34 – 38, DOI: 10.1109/IIPHDW.2019.8755409.

